Micro-scale measurement and modeling of stress in silicon surrounding a tungsten-filled through-silicon via

Ryan P. Koseski,[1,a)] William A. Osborn,[1,b)] Stephan J. Stranick,[2] Frank W. DelRio,[1] Mark D. Vaudin,[1] Thuy Dao,[3] Vance H. Adams,[4] and Robert F. Cook[1]
[1]*Ceramics Division, Material Measurement Laboratory, National Institute of Standards and Technology, Gaithersburg, Maryland 20899, USA*
[2]*Surface and Microanalysis Division, Material Measurement Laboratory, National Institute of Standards and Technology, Gaithersburg, Maryland 20899, USA*
[3]*RF, Analog, and Sensor Group, Freescale Semiconductor, Austin, Texas 78735, USA*
[4]*RF, Analog, and Sensor Group, Freescale Semiconductor, Tempe, Arizona, 85284, USA*

(Received 25 July 2011; accepted 22 August 2011; published online 11 October 2011)

The stress in silicon surrounding a tungsten-filled through-silicon via (TSV) is measured using confocal Raman microscopy line scans across the TSV both before and after etch removal of an oxide stack used as a mask to define the TSV during fabrication. Stress in the silicon arose in response to both athermal deposition and thermal expansion mismatch effects. The complex three-dimensional stress and strain field in silicon surrounding the TSV is modeled using finite element analysis, taking into account both athermal and thermal effects and the elastic anisotropy of silicon. Comparison of the measurements and model results shows that no one component of the stress tensor correlates with the Raman peak shift generated by the deformed silicon. An analysis is developed to predict the Raman shift in deformed silicon that takes into account all the components of the stress or strain tensor; the results of the model are then used as inputs to the analysis for direct comparison with measured peak shifts as a function of distance from the TSV. Good agreement between the measured and predicted peak shifts is obtained for the case of the intact oxide stack. A discrepancy between the measured and predicted shifts was observed adjacent to the TSV with the oxide stack removed; further modeling suggests the discrepancy is explained by the formation of a small void at the TSV-silicon interface during etching. The combined measurement-modeling approach serves to both validate the model, in this case for TSV design, and to extend the measurement capability of confocal Raman microscopy to complex stress fields. © *2011 American Institute of Physics*. [doi:10.1063/1.3644971]

I. INTRODUCTION

Three-dimensional (3-D) integration of silicon (Si) microelectronic devices enables enhanced device performance and new device functionality.[1] A 3-D integrated device consists of individual Si dies "stacked" on top of each other, with vertical electrical interconnection between the dies achieved by electrodes on the die faces. The performance advantages of this scheme include: (i) a significant reduction of the volume required for die packaging because only the footprint of the die is required for electrical connections; (ii) a reduction in device power consumption and an increase in interconnection bandwidth as wiring between dies and packaging is minimized; and (iii) lower cost because packaging is minimized.[2–5] Additionally, new functionality is gained by combining heterogeneous device elements, such as logic with memory,[6] logic with microelectromechanical systems (MEMS),[7] or logic with optoelectronic systems.[8]

A key enabling component of 3-D integration is the "through-silicon via" (TSV)—a metallic conducting via passing through the Si die that provides the electrical connection between the active front side of the die and the backside where interconnection with other dies is made.[1] TSVs are fabricated by deep reactive-ion etching (DRIE) of Si to form via trenches,[9,10] often followed by deposition of a side-wall diffusion barrier, typically silicon oxide or titanium nitride, followed by deposition of the metal, either copper by plating onto a seed layer, or poly-Si or tungsten (W) by chemical vapor deposition (CVD).[11–14] Typical via dimensions are a few micrometers in width and many tens of micrometers in length through the substantially thinned Si die.

Independent of the fabrication method, composition, or geometry of a TSV is the generic fact that the TSV materials are different from the surrounding Si and have different thermomechanical properties. As a consequence, stress fields can be generated in the Si, TSV, and surrounding interconnection structures by the thermal expansion mismatch effects between the Si and the TSV materials upon cooling from elevated temperature TSV deposition conditions or from other elevated temperatures during device fabrication.[15,16] Such thermal stresses may be superposed on athermal stresses generated prior to cooling in reaction to strains generated in the TSV material during deposition. The net stress field can significantly alter device fabrication yield and operational performance in two ways: (i) The stresses may drive delamination and fracture in the TSV or surrounding interconnection structures,

[a)]Present address: The Pennsylvania State University, State College, Pennsylvania, 16802, USA.
[b)]Author to whom correspondence should be addressed. Electronic mail: william.osborn@nist.gov.

leading to electrical opens or shorts,[17,18] and (ii) the stresses will modify the mobility of carriers in the surrounding Si, altering the electrical characteristics of the device.[19,20] Since both of these effects will be influenced by the thermal cycling associated with device operation, these two factors will also be device reliability concerns.

In order to set design and fabrication ground rules for 3-D integrated devices, such as TSV dimensions, pitch, and temperature excursions allowed during device fabrication and operation,[21,22] validated models of the stress fields associated with TSVs are required. Such models enable devices to be optimized for maximum yield and reliability with minimized empirical trials of candidate new devices or operating conditions. Here we validate such a model using a rectangular W-filled TSV as a test vehicle. This test vehicle is significant because the 3-D extent of the TSV generates a complex stress field that is difficult to describe with simple analytical models but is also typical of 3-D integrated devices. Models of the stress field, generated by finite element analyses (FEAs) of the material surrounding the TSV, are used to predict the stress-driven changes of the Raman scattering spectrum in the surrounding Si for direct comparison with measurements obtained by confocal Raman microscopy (CRM). The work extends a previous comparison of the CRM and electron backscattered diffraction measurements of stress using a wedge indentation with a much simpler, almost two-dimensional, stress field.[23]

II. EXPERIMENTAL AND ANALYTICAL METHODS

A. TSV fabrication

The TSV test structure was fabricated in a single crystal Si (001) wafer on which a 2.5 μm thick phosphosilicate glass (PSG) and un-doped silicate glass (USG) trilayer (PSG-USG-PSG) film was first deposited by CVD at 380 °C as an interlayer dielectric base layer (termed ILD0). This film was subsequently capped with a 200 nm silicate film generated by plasma enhanced CVD from a tetraethylorthosilicate (TEOS) precursor at 425 °C. A photoresistive film was deposited on the combined ILD0-TEOS oxide stack and patterned with i-line photolithography, such that after development 2.5 μm wide and 30 μm long openings were formed, exposing the oxide stack with the symmetrical axes of the rectangular opening aligned with the Si ⟨110⟩ directions. The oxide stack was subsequently plasma etched to the silicon surface and the photoresist removed by plasma stripping to leave the oxide stack as a hardmask. The TSV trench was then etched into the Si using the DRIE process with alternating polymer deposition and silicon etching steps to a nominal depth of 80 μm. The DRIE process undercut the oxide hardmask by 0.5 μm on each side to leave a 3.5 μm wide TSV trench. After cleaning, the etched trench was filled with W by CVD at 425 °C using WF_6 precursor. The triaxial athermal deposition stress generated in the W as a consequence of the CVD process was determined to be 1.4 GPa by extrapolating wafer curvature measurements of this CVD process. Chemical mechanical polishing was then used to remove excess W from the surface down to the TEOS layer to leave the W feature extended above the Si surface and flush with

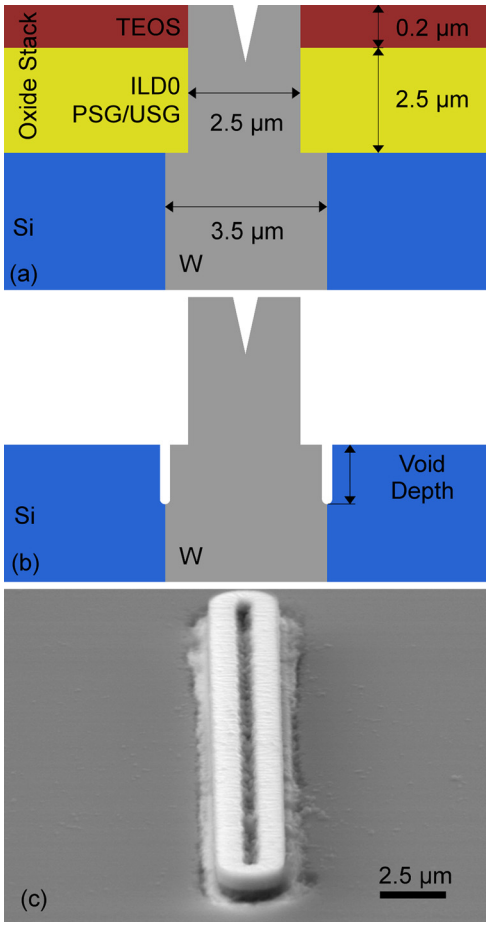

FIG. 1. (Color online) The TSV test vehicle. (a) Schematic diagram of as-fabricated structure with the oxide stack. (b) Schematic diagram of chemically-etched structure with the oxide stack removed and a small void generated at the Si-W interface. (c) SEM image of the etched structure.

the remaining un-etched ILD0-TEOS stack. A schematic diagram of the completed structure is shown in cross-section in Fig. 1(a). Following the initial non-destructive CRM measurements, the ILD0-TEOS oxide stack was removed using a chemical etch consisting of rinsing in a buffered hydrofluoric acid solution (6:1 NH_4F:HF) for 10 min, followed by a deionized water rinse. A schematic cross-section of the etched structure is shown in Fig. 1(b). With the oxide stack removed, the Si surface was exposed and the elevated W was easily observed, as shown in the scanning electron microscope (SEM) image of Fig. 1(c). A surface localized seam in the center of the elevated TSV material in the W is visible. Also visible are some regions of apparent separation between the Si and W at the interface on the surface, although the depth of this void is not evident. The sample (x_s, y_s, z_s) and crystallographic (X, Y, Z) axes of the TSV and Si are illustrated in Fig. 2.

B. FEA simulation

FEA simulations were performed to model the residual stress state in the Si surrounding the TSV. Stress in the model was induced in the Si as a consequence of thermal expansion mismatch between the Si, oxide stack, and W upon cooling from the elevated deposition temperatures and

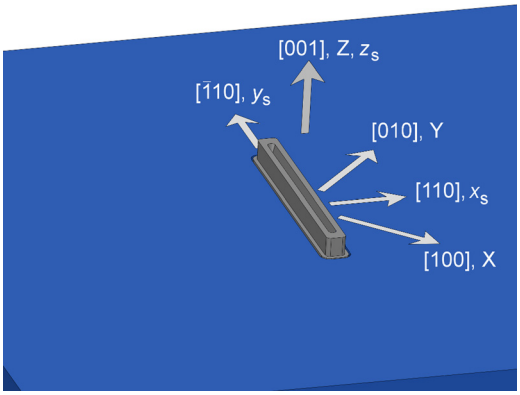

FIG. 2. (Color online) Experimental sample (x_s, y_s, z_s) and crystallographic (X, Y, Z) axes of the TSV structure.

as a consequence of the athermal stresses generated in the W during deposition.[24] The stress was generated in reaction to constraint of the imposed thermal and athermal strain mismatches by enforcing adherent interfaces between the different materials. In the simulations, interfaces were considered perfectly adhered unless specifically treated otherwise to preserve the strain state across the interface. The thermomechanical properties of the materials used in the simulations are given in Table I. The Si was treated as elastically anisotropic and the three independent components of the elastic stiffness tensor, C_{IJ}, are given; the oxides and W were treated as elastically isotropic with Young's modulus, E, Poisson's ratio, ν, and the coefficient of thermal expansion (CTE), α. Also given in Table I are the strain-free reference temperatures, T_{ref}, away from which materials accumulate strain energy upon cooling due to CTE mismatch effects. The reference temperatures for the CVD materials were taken as the CVD deposition temperatures, and the reference temperature for the Si was taken as the deposition temperature of the first CVD step.

The two-fold symmetry of the TSV was utilized in the development of the model to reduce the computational resources required. This was accomplished by enforcing symmetric (reflective) boundary conditions at the x_s-z_s and y_s-z_s planes that intersect the center of the TSV. The results of the models presented have dimensions of 50 μm in the x_s- and y_s-directions and 80 μm in the z_s direction. An additional 7.5 μm extent in the x_s- and y_s-direction was modeled to reduce the shear effects of the strained thin films near the free edges of the model, but these regions are not presented. Convergence of the stress field around the TSV was checked

TABLE I. Bulk material properties used in the FEA model.

Layer		Elastic modulus C_{IJ} or E (GPa)	Poisson's ratio, ν	CTE, α ($\times 10^{-6}$ K^{-1})	T_{ref} (°C)
Si	C_{11}	166	—	2.62	380
	C_{12}	64			
	C_{44}	80			
W		411	0.29	4.6	425
ILD0		56	0.2	1	380
TEOS		65	0.25	0.6	425

at larger model dimensions; however, the effects of the TSV on the Si substrate stress field were deemed negligible for models larger than 50 μm in the x_s- and y_s-directions. The bottom plane of the model was fixed in the z_s direction to simulate attachment to an effectively rigid wafer. The model was meshed using quadratic tetrahedral elements. An iterative adaptive remeshing procedure was used to refine the mesh using a von Mises stress error indicator as the remeshing criteria. This process yielded stress field solutions with 99.8% of the elements with an error estimate of less than 0.5%. By visual inspection, the remaining 0.2% of the elements were at or near the singularity at the triple junction between the Si-W-ILD0.

In addition to the stresses generated by CTE mismatches, the athermal stress of the CVD-deposited W was included in the model. For an isotropic material, an arbitrary athermal stress, σ_{athermal}, can be generated by applying a temperature offset, $\Delta T_{\text{athermal}}$, given by

$$\Delta T_{\text{athermal}} = \frac{\sigma_{\text{athermal}}(1-2\nu)}{E\alpha}, \tag{1}$$

to the nominal temperature of the simulation. Thus, to account for the CTE mismatch and athermal stresses, the simulation temperature for the Si and oxide stack was 25 °C and the simulation temperature for the W elements was −286 °C. For simulations neglecting athermal stresses, the nominal simulation temperature and the actual simulation temperature are the same.

Some simulations were performed with a void of finite depth (measured from the top surface of the Si as indicated in Fig. 1(b)) at the Si-W interface. All voids were generated by centering a 10 nm wide rectangle and sweeping it along the path formed by the intersection of the Si and W. The termination of the void was a 5 nm radius semicircle. To improve the performance of the remeshing procedure, the void termination singularity was isolated using a 100 nm dodecagon. Iterative remeshing was also used and, similarly to the previously discussed findings, the majority of elements with error indicators greater than 0.5% were near the singularity at the void termination.

C. CRM measurements

The CRM measurements were performed using a custom system similar to that previously used.[23,25] The excitation radiation was provided by a diode laser generating a 405 nm wavelength light. The laser beam was passed through a collimator and a polarizing filter to generate a polarized Gaussian beam. The light was focused on the sample using a 60× oil immersion high numerical aperture lens (N.A. = 1.4) to a spot size of approximately 140 nm. The scattered Raman light was collected through the lens, directed through a high pass filter with an absorption edge at 407 nm, and analyzed with a 0.5 cm^{-1} resolution spectrograph. Both the illumination and collection polarization filters were oriented with the electric field vector along the y_s axis: using the Porto notation, the laser was polarized in a $z_s(y_s, y_s)\bar{z}_s$ (backscattering) orientation. A piezoelectric driven x-y stage with closed loop control with 10 nm resolution allowed for scanning of the

sample. Penetration of laser light varies strongly with wavelength, and the information depth for the 405 nm excitation wavelength in Si is approximately 50 nm to 100 nm.[26] The CRM line scans were conducted along the x_s axis (see Fig. 2), perpendicular to the long dimension of the TSV features with 512 steps over 80 μm, resulting in a step size of 156 nm. Spectra were collected with a constant laser intensity and a constant integration time of approximately 1 step sec^{-1}, yielding a signal to noise ratio ≈30:1.

Attention was focused in the collected spectra on scattering of the light by Si longitudinal optical phonons, which have a characteristic Raman scattering frequency, ω_0, of approximately 520 cm^{-1} in the unstressed state.[27] As a first approximation, tensile stresses shift this frequency to smaller values and compressive stresses to larger values; this will be considered in detail in the following section. The initial CRM measurements were performed on the Si surrounding the unaltered TSV feature through the 2.7 μm oxide stack. The stack did not appear to adversely affect the Raman information obtained from the Si substrate since the characteristic Si peak was of the same intensity and line shape as measured on a bare Si surface. There was a contribution to the spectrum in the form of an "amorphous hump" at higher wavenumbers in the Raman spectrum originating from interaction with the oxide material, but that did not appear to affect the shape of the crystalline Si Raman peak as reflected by the fitting parameters of a Pearson VII fitting algorithm. With the multiple oxide layers removed, the CRM measurements of the exposed silicon were repeated along the x_s axis.

D. Raman shift prediction

A general methodology is developed here to enable the comparison of results of the FEA simulations and the CRM. Ideally, stress is the comparative metric of choice because it is intuitively understood and directly applicable to material properties along with device performance and reliability relationships. An FEA provides the stress and strain at integration points in each element in full tensor form, however, CRM only provides a scalar Raman shift at each measurement point. Despite being an easily applied measurement technique, this reduction in information makes converting CRM experimental data to determine stress problematic, particularly when the general stress state is unknown or not easily predicted by analytical solutions. The method employed here to enable comparison is to use the calculated elastic strain tensor from the FEA simulations to predict a Raman shift that can be compared directly to the CRM data.

In previous experiments in which CRM was utilized as the stress measurement technique, the method of analysis was to interpret the shift of the Raman peak as a proportional response to strain, and subsequently, stress.[28–30] To compare FEA results to CRM results, the reverse calculation was utilized here; that is, the shift of the Raman peak was predicted from a FEA elastic strain state. The FEA strain state was modeled in the sample axes and the elastic strain tensor was given by,

$$\boldsymbol{\varepsilon}_s = (\varepsilon_{kl})_s, \tag{2}$$

and was rotated from the stage axes (x_s, y_s, z_s) to give the strain tensor, ε_{kl}, in the crystallographic axes (X, Y, Z) by the transformation,

$$\varepsilon_{ij} = a_{ik}\varepsilon_{kl}a_{lj}, \tag{3}$$

where the Einstein repeated-index summation convention is used, and

$$a_{ik} = a_{lj}^{\mathrm{T}} = \begin{bmatrix} \cos\theta & -\sin\theta & 0 \\ \sin\theta & \cos\theta & 0 \\ 0 & 0 & 1 \end{bmatrix}, \tag{4}$$

is the rotation matrix about the common [001] z_s and Z axes, and T indicates transpose. In Eq. (4), θ is the angle between the x_s and X axes; here $\theta = 45°$. The strain tensor in the crystallographic axes was used to calculate the change in the Raman spectrum from the unstrained state in two steps; the first requiring the change in frequency of the Raman phonon modes contributing to the spectrum and the second requiring the change in intensity of these modes.

In Si, the characteristic peak in the Raman spectrum is the summation of three overlaying peaks,[27] which in the unstrained state have a degenerate Raman frequency, ω_0. The application of non-hydrostatic strain splits the degeneracy into three frequencies, $\omega^{(\alpha)}$, $\alpha = 1$, 2, and 3, given by

$$(\omega^{(\alpha)})^2 = \omega_0^2 + \lambda^{(\alpha)}, \tag{5}$$

where $\lambda^{(\alpha)}$ is one of three eigenvalues of the secular equation involving the strain tensor in the crystallographic axes found using,

$$\begin{vmatrix} p\varepsilon_{11} + q\varepsilon_{22} + q\varepsilon_{33} - \lambda & 2r\varepsilon_{12} & 2r\varepsilon_{13} \\ \cdot & q\varepsilon_{11} + p\varepsilon_{22} + q\varepsilon_{33} - \lambda & 2r\varepsilon_{23} \\ symm & \cdot & q\varepsilon_{11} + q\varepsilon_{22} + p\varepsilon_{33} - \lambda \end{vmatrix} = 0, \tag{6}$$

where p, q, and r are the phonon deformation potentials related to the electronic polarizability, χ_{ij}, by,[29]

$$p = m^{-1}\frac{\partial \chi_{ii}}{\partial \varepsilon_{ii}} = -1.85\omega_0^2,$$

$$q = m^{-1}\frac{\partial \chi_{ii}}{\partial \varepsilon_{jj}} = -2.31\omega_0^2,$$

$$r = m^{-1}\frac{\partial \chi_{ij}}{\partial \varepsilon_{ij}} = -0.71\omega_0^2, \tag{7}$$

where m is the reduced mass of the two silicon atoms in the primitive unit cell. For small strains the frequency shifts, $\Delta\omega^{(\alpha)} = \omega^{(\alpha)} - \omega_0$, for each mode are small, so that to first order Eq. (5) can be written as,

$$\Delta\omega^{(\alpha)} = \frac{\lambda^{(\alpha)}}{2\omega_0}. \tag{8}$$

Hence, the first step in predicting the Raman spectrum in the strained state was to determine ω_0 from measurements on an unstrained reference material, calculate p, q, and r from Eq. (7), determine the three eigenvalues, $\lambda^{(\alpha)}$, of Eq. (6) using the FEA strain tensor, ε_{ij}, and thence calculate the changes in frequency, $\Delta\omega^{(\alpha)}$, for the three modes from Eq. (8).

The three eigenvectors of the secular equation, $\boldsymbol{\xi}^{(\alpha)} = [\xi_1, \xi_2, \xi_3]^{(\alpha)}$, determine the intensity contribution of each mode to the overall spectrum as a function of the polarization directions of the incident and scattered light. Three unstrained Raman tensors, $\boldsymbol{R}_1$, $\boldsymbol{R}_2$, and $\boldsymbol{R}_3$, couple intensity to polarization for the three optical phonon modes in diamond cubic Si, and are given by,

$$\boldsymbol{R}_1 = \begin{bmatrix} 0 & 0 & 0 \\ 0 & 0 & d \\ 0 & d & 0 \end{bmatrix}, \boldsymbol{R}_2 = \begin{bmatrix} 0 & 0 & d \\ 0 & 0 & 0 \\ d & 0 & 0 \end{bmatrix}, \boldsymbol{R}_3 = \begin{bmatrix} 0 & d & 0 \\ d & 0 & 0 \\ 0 & 0 & 0 \end{bmatrix}, \tag{9}$$

where the indices (1, 2, 3) are linked to the crystallographic axes (X, Y, Z). The material constant, d, related to the scattering efficiency is the same in each tensor. In the strained state, the intensity contribution is not the same for each mode and the three strained Raman tensors, $\boldsymbol{R}^{(\alpha)}$, $\alpha = 1$, 2, and 3, for the shifted modes are sums of the unstrained tensors weighted by the components of the three eigenvectors,

$$\boldsymbol{R}^{(\alpha)} = \xi_1^{(\alpha)}\boldsymbol{R}_1 + \xi_2^{(\alpha)}\boldsymbol{R}_2 + \xi_3^{(\alpha)}\boldsymbol{R}_3. \tag{10}$$

The intensity of each shifted mode, $I^{(\alpha)}$, is related to the polarization vectors of the incident light, $\boldsymbol{e}_{(\mathrm{i})}$, and scattered light, $\boldsymbol{e}_{(\mathrm{s})}$, by

$$I^{(\alpha)}(\boldsymbol{e}_{(\mathrm{s})}, \boldsymbol{e}_{(\mathrm{i})}) = I_0\left(\boldsymbol{e}_{(\mathrm{s})} \cdot \boldsymbol{R}^{(\alpha)} \cdot \boldsymbol{e}_{(\mathrm{i})}^T\right)^2, \tag{11}$$

where I_0 is a constant that includes the experimental variables such as laser intensity, wavelength, and integration time. Polarization vectors are defined in the crystallographic axes [X, Y, Z], as shown in Fig. 2, and where $\boldsymbol{e}_{(\mathrm{i})} = \boldsymbol{e}_{(\mathrm{s})} = [1\bar{1}0]$. (There is some depolarization in the scattered light that has been addressed in previous work,[31] however the majority of the scattered light is assumed to be polarized in the same direction as the incident light for these calculations.) Hence, the second step in predicting the Raman spectrum was to use the eigenvalues to determine the eigenvectors of the secular equation, $\boldsymbol{\xi}^{(\alpha)}$, from Eq. (6), calculate the strained Raman tensors, $\boldsymbol{R}^{(\alpha)}$ from Eq. (10), and thence, calculate the intensity, $I^{(\alpha)}$, of each of the three shifted modes from Eq. (11). For the crystallographic orientation described here, Eq. (11) simplifies to,

$$I^{(\alpha)}([1\bar{1}0], [1\bar{1}0]) = I_0\left(-2d\xi_3^{(\alpha)}\right)^2, \tag{12}$$

and is the orientation of maximum intensity.

The Raman peaks for the individual modes separate under various strain states. However, under the constraint of small strains, the peaks do not fully resolve experimentally, and the observed spectrum appears as a net single, shifted, and broadened peak. Thus, the two previous steps were combined to predict the net shift, $\Delta\omega_{\mathrm{obs}}$, by weighting the shifts of the individual modes by their intensities,

$$\Delta\omega_{\mathrm{obs}} = \frac{\sum_{\alpha=1}^{3} I^{(\alpha)}\Delta\omega^{(\alpha)}}{\sum_{\alpha=1}^{3} I^{(\alpha)}}. \tag{13}$$

It is a simple exercise to show that this calculation predicts no shift for a hydrostatic stress and a shift of 1 cm^{-1} for a uniaxial stress of −435 MPa along the [110] direction, which is the linear constant of the accepted stress to shift relationship in the case of uniaxial stress.[29,32–34]

III. RESULTS

A. Oxide stack intact

The results of the FEA simulation of the quarter-symmetry TSV structure with the oxide stack still present are shown in Fig. 3 as contour plots of the predicted Raman shift in the Si. The shifts are taken relative to an unstrained frequency of $\omega_0 = 520.9$ cm^{-1}. Figure 3(a) shows the entire simulation, with the non-Si materials uniformly colored as in the scheme of Fig. 1; these colors do not indicate predicted Raman shifts. In most of the simulated volume of Si the predicted shift is close to zero. Close to the TSV and oxide stack, there are large gradients in the predicted shift on a length scale much larger than either the width (x_s-dimension) of the TSV or thickness (z_s-dimension) of the oxide stack. This gradient is particularly strong approaching the Si-W-ILD0 triple junction. Figure 3(b) is a magnification of Fig. 3(a) with the oxide stack hidden so that the contours on the top Si plane (x_s-y_s) are visible. The variation in the predicted shift in the y_s direction along the x_s axis is negligible, suggesting that the CRM line scans performed in the x_s direction away from the TSV will not be sensitive to the exact y_s position around the center of the TSV.

Figure 4 shows a plot of the measured shift from a CRM line scan along the x_s axis. The shifts were determined relative to a reference spectrum obtained at $x_s = y_s = 30$ μm. The FEA simulations indicated that at locations farther than this from the TSV the predicted shift was invariant and smaller than the resolution of the measurements, which was approximately ± 0.05 cm^{-1}. Far from the TSV, the measured shift was zero. On approach to the TSV, the shift significantly increased to greater than 1 cm^{-1} over a length scale of about 10 μm. Also shown in Fig. 4 are the components of the stress tensor along the same line obtained from the FEA simulation. For the purposes of comparison only, the Raman shift and stress axes are linked using the uniaxial stress to Raman shift of −435 MPa/cm^{-1}. Examining each individual component of the stress tensor shows the expected trends: away from the

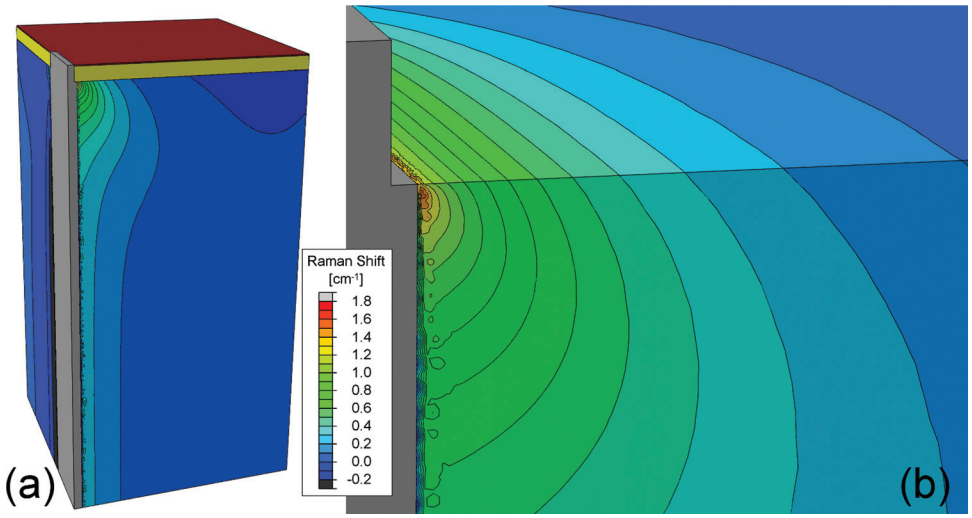

FIG. 3. (Color) Contour plot of the calculated Raman shift, $\Delta\omega$, of the silicon. The via (gray) is shown in both (a) and (b), but the ILD0 (yellow) and TEOS (red) are hidden in (b) to reveal the contours on the top surface of the silicon.

TSV, σ_{x_s} is tensile in response to the contraction of the W, but near the TSV the force from the vertical contraction of the W dominates and causes σ_{x_s}, σ_{y_s}, and σ_{z_s} to be compressive and generates an appreciable shear, $\tau_{x_s z_s}$. Due to symmetry, $\tau_{x_s y_s}$ and $\tau_{x_s z_s}$ are effectively zero. The four non-zero components of the stress tensor vary in magnitude, sign, and length scale adjacent to the TSV, indicating a complex stress state, and thus uni- or equibiaxial stress interpretations of the CRM data would be incorrect. A comparison of the CRM measurements and the stress components in Fig. 4 shows this to be the case: There is a lack of correlation between the CRM data and any individual stress tensor component.

Using the analysis method developed in Section II D, the strain tensors along the x_s axis were used to predict the Raman peak shifts for the CRM line scan shown in Fig. 4. Figure 5 shows a plot of the measured shifts (symbols) repeated from Fig. 4 and the predicted shifts using the combined athermal and thermal contributions to strain (solid line). Notwithstanding the scatter in the experimental data, there is good agreement between the measurement and the prediction using the combined contributions. A second simulation where the athermal contributions of the W were neglected by removing $\Delta T_{\text{athermal}}$ results in a large underestimation of the magnitude of the Raman shift near the TSV (dashed line).

B. Oxide stack removed

The CRM measurements and FEA simulations were also performed for the case in which the oxide stack was removed. The CRM measurements for the oxide stack removed case are shown in Fig. 6. Upon approaching the TSV from $x_s > 0$, the shift increased over a 10 μm length scale, similar to the oxide stack intact case (Fig. 5), but the magnitude of the trend was approximately half that of the intact case, reaching a peak shift of approximately 0.8 cm^{-1} compared with 1.6 cm^{-1}. A similar trend is observed for $x_s < 0$, however, the magnitude was even smaller, reaching a peak shift of approximately 0.4 cm^{-1}. At smaller length scales, as shown in the inset of Fig. 6, a deviation from the increasing trend was observed for $x_s < 0$, with the shift decreasing from the peak value about 2 μm from the TSV.

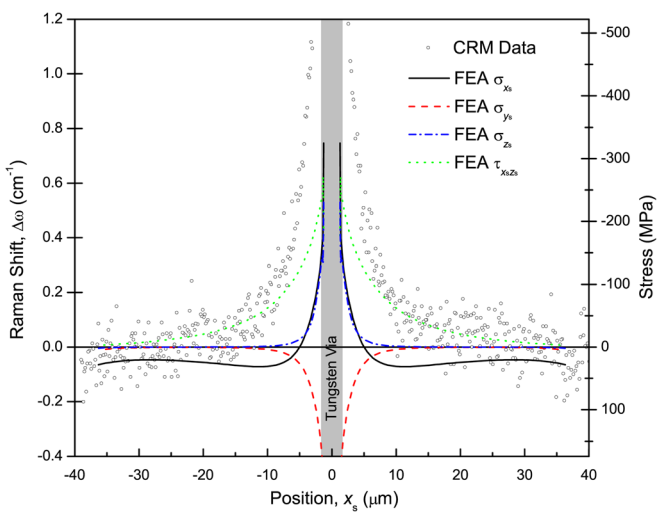

FIG. 4. (Color online) Plot of stress and experimental CRM values vs position along the x_s axis defined in Fig. 2. Four of the six components of the stress tensor for the nodes directly on the x_s axis are plotted;$\tau_{x_s y_s}$ and $\tau_{x_s z_s}$ are essentially zero for all the plotted positions and are not shown.

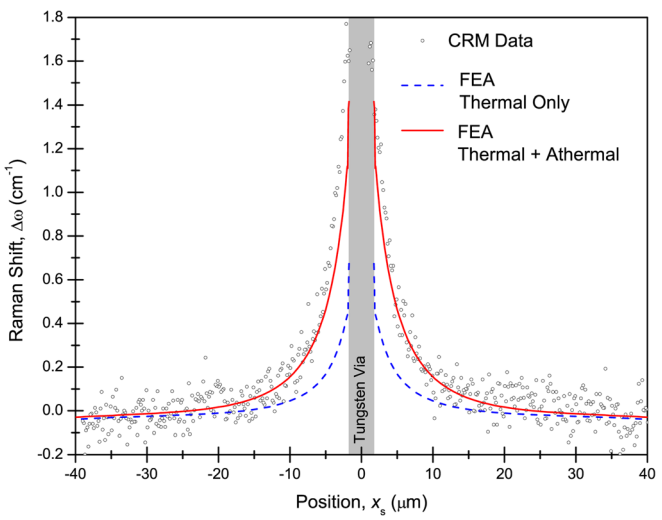

FIG. 5. (Color online) Plot of Raman shift measured by CRM (symbols) vs position relative to the TSV center along the x_s axis for the oxide on structure. The Raman shift calculated from the FEA elastic strain tensor is shown for both the thermal + athermal and thermal only stresses.

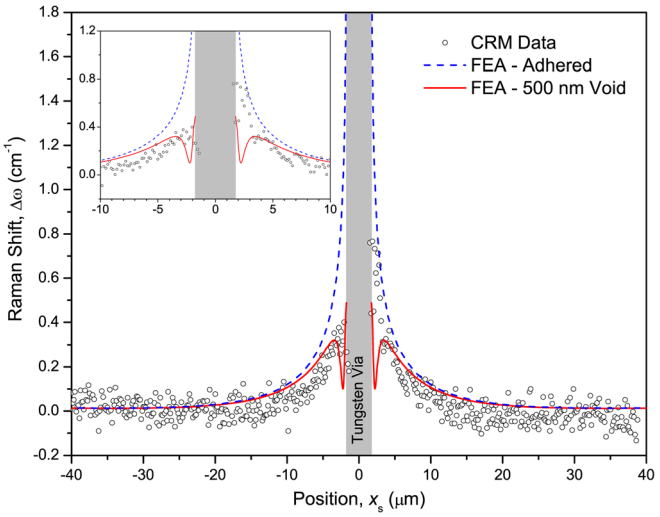

FIG. 6. (Color online) Plot of Raman shift measured by CRM (symbols) vs position relative to the TSV center along the x_s axis for the oxide removed structure. The predicted Raman shifts using six component strain tensors from the FEA simulations are superposed.

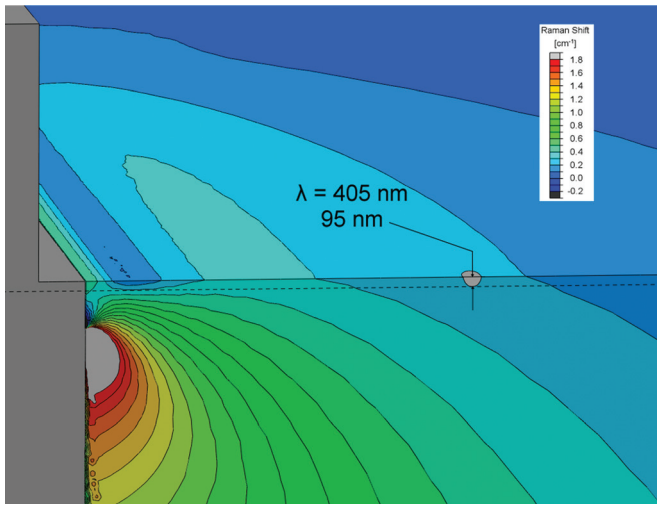

FIG. 7. (Color) Contour plot of the predicted Raman shift for the silicon surrounding the TSV (gray at left) with a 500 nm deep void introduced at the Si-W interface. The labeled ellipse represents an approximation of the information volume for the 405 nm CRM. A dashed line at 95 nm deep shows that near the Si-W interface the information volume intersects a strong gradient in the predicted Raman shift.

The predicted Raman shift along the x_s axis, calculated from FEA simulation of the oxide stack removed case, is shown in Fig. 6 as the dashed line. Similar to the oxide stack intact simulation, perfectly adherent interfaces were enforced and both thermal and athermal stresses were used. The FEA simulations showed that removing the 2.7 μm thick oxide stack made only small changes to the overall stress state and the predicted shift caused by the 80 μm deep TSV. Whereas the oxide stack intact model slightly underestimates the magnitudes of the shifts, the calculated shifts for the oxide stack removed case appreciably overestimate the observed magnitudes. This overestimate is most readily apparent in the inset of Fig. 6 that magnifies the region near the TSV.

One possible explanation for the reduction in magnitude of the CRM shift and the lack of agreement between the measured and predicted shift values is the release of strain energy by the partial delamination of the Si-W interface. To investigate this possibility, FEA was used to simulate the stress in the structure with voids at the Si-W interface. Voids of several depths (100 nm, 250 nm, 500 nm, 1.0 μm, and 2.0 μm) were modeled and a depth of 500 nm was found to be the closest fit to the CRM data. The predicted Raman shifts for the FEA simulation of the 500 nm void are also presented in Fig. 6 as the solid line. These predictions more closely match the magnitudes of the measured Raman shifts for all x_s and the downward trend for $x_s < 0$ close to the TSV is also captured. Figure 7 shows a contour plot of the predicted Raman shift in the Si adjacent to the TSV with an interfacial void 500 nm deep. A comparison of Fig. 7 and Fig. 3(b) shows that the effect of the void is to significantly alter the shift field near the surface adjacent to the Si-W interface.

IV. DISCUSSION

The analysis of the TSV test structure used in this study is an excellent example of the power of CRM as a strain measurement technique as well as the care that must be taken in interpreting the results. CRM has previously been used to probe the strain field around a wedge indentation,[23] and for that work a uniaxial stress adjacent to the indentation was shown to be an adequate description of the strain field. Because of the simple strain state near the surface, a scalar relation between the Raman shift and stress (–435 MPa/cm^{-1}) could be used. This methodology is similar to the analytical comparisons of stress in the edge force model of Hu[32,33] or micro-dogbone-like uniaxial tension,[35] among others in published micro-Raman results.[31,36] Anastassakis *et al.* has argued[28] that the selectivity of phonons scattering from light polarized perpendicular to a component of strain causes the Raman shift of light polarized in the y_s direction to be dominated by strains in the x_s direction, especially when a low N.A. objective is used. Under any of these interpretations, the trend of the CRM measurements should be exhibited by the x_s components of the strain tensor from the FEA simulation. Such a comparison is shown in Fig. 4, and although the variation of peak shift with distance from the TSV is similar to the trend of the major stress components, not one of the σ_{x_s}, σ_{y_s}, or σ_{z_s} is deterministic. In contrast, the predicted Raman shift from the thermal + athermal simulation (Fig. 5) is an excellent match to the CRM measurements for the oxide stack intact case. Even though the rigorous method for predicting Raman shifts described in Sect. II D is always applicable, the surface stress states for the studies mentioned could be well described using simplified strain states, which made the rigorous treatment unnecessary. However, the TSV studied here cannot be simplified and thus, the full analysis was necessary.

In practice, the analysis approach used here is reversed from the normal method of interpreting strain (and hence, stress) from a measured Raman shift. The shift to strain approach is only applicable for cases where the strain state is known to be simple, and the CRM measurements provide no

indication for when this assumption is not valid. If a direct conversion of the Raman shift to stress had been made using the uniaxial translation of -435 MPa/cm^{-1}, the compressive stress surrounding the TSV would have been overestimated by a factor of 2. The scalar Raman shift is a non-unique function of all six components of the strain tensor, and thus attempting to decompose the scalar into components of the tensor is an error prone procedure. Instead, by simulating the structures of interest to obtain strain tensors and then predicting the Raman shift, correlation between the CRM measurements and the predicted shifts can serve as a confirmation that the simulated strain state is correct.

To efficiently execute this type of reverse analysis, a sensible approach is to integrate the Raman shift prediction described in Sec. II D into the FEA package. Advanced commercial FEA packages permit users to specify new field outputs, and by implementing the strain to Raman shift calculation as a field output, the user can view the calculated Raman shift in the same way other invariant field outputs are viewed. In practice, there are several important considerations to this approach. First, the p, q, and r values from Eq. (7) are crystal orientation dependent, and thus the strain tensor must be rotated into the crystal orientation. Although this can be done programmatically, transforming the strain tensor into an arbitrary orientation is typically simple for FEA packages and thus programmatic implementation of Eqs. (2)–(4) is unnecessary. The second consideration is the choice of the field output to use as the input to the Raman shift calculation. The components of the stress tensor are commonly examined and are thus readily accessible. By using the compliance tensor, stress can be converted to strain, but this step is also unnecessary if the elastic strain tensor is an available field output. By implementing this approach, the predicted Raman shifts in this work were computed for every integration point within the Si entirely inside the FEA package, significantly reducing the effort required to make direct comparisons between simulations and measurements.[37]

Figure 5 demonstrates the usefulness of combining the FEA simulations with the CRM measurements. Most of the material properties used for the FEA simulation (Table I) are readily available; however, the athermal stress of the W deposition is very process dependent. When the athermal strain contribution is neglected, the simulated strains surrounding the TSV are incorrect (too small), and thus, the predicted Raman shift does not match the CRM measurements—indicating the thermal only simulation is incorrect. However, the strong correlation between the predicted thermal + athermal Raman shifts and the measured CRM shifts confirms that a 1.4 GPa athermal deposition stress in the W is reasonable. It is beyond the scope of this set of experiments to precisely determine what the athermal stress is for the W deposition, but the results confirm that the stress is present, measurable, and of the expected magnitude. It is not clear at this point whether these techniques can be applied in a quantitative fashion to determine this value in the future.

Careful examination of Fig. 6 reveals a lack of symmetry in the CRM data that is not exhibited by the FEA simulations. The simulations assumed quarter symmetry and thus the FEA data in Figs. 4–6 is simply mirrored about $x_s = 0$, but the asymmetry in the CRM data indicates this may not always be a valid assumption. For cases where perfect adhesion of the interfaces is preserved, the assumed symmetry is correct; however, the TSV test structure is unlikely to have perfectly uniform and adhered interfaces. Evidence of a void formation at the Si-W interface can be seen in Fig. 1(c). Although the micrograph is not conclusive, there is reason to believe that a non-uniform void that the quarter symmetry of the simulation does not account for may form. The driving force for the growth of the proposed void at the Si-W interface is the relief of strain energy in both the Si and W. Once a void forms at the surface and grows down an interface, the depth of the void will be determined by the balance of the strain energy released to the surface energy created. However, the growth of a void on one side of the TSV would relieve strain energy on both sides of the TSV by bending the upper part of the W. The quarter symmetry model developed for this work is not capable of capturing this type of behavior; however, the disparity between the calculated and measured shifts in Fig. 6 indicate that this behavior may be occurring. The CRM data on the right side ($x_s > 0$) falls between the adhered and 500 nm void simulations, which is easily observed in the inset of Fig. 6. More importantly, the trend of the CRM data is continually increasing up to the Si-W interface, and the medium range decrease that the 500 nm void simulation predicts is not observed. In contrast, the left side CRM data ($x_s < 0$) does decrease approaching the Si-W interface and the predicted shift magnitude is much closer to the measured values. This observation supports the conclusion that the void only formed on one side of the TSV. Furthermore, the intermediate magnitude of the CRM data is consistent with this explanation because the Si on the right side of the TSV in Fig. 6 would experience identical strain in the z_s direction with a reduction in stress in the x_s direction. Regardless of the symmetry of the void, the scalloped nature of the interface that results from the DRIE process is likely to provide excellent traction between the interfaces in the z_s direction, therefore, a void of significant size would be required to relieve strain energy from the z_s contraction. However, without significantly more information about the geometry and mechanics of the interface, this hypothesis cannot be tested with a lower symmetry model.

In addition to providing insight into the validity of the simulation, the calculation of the shift field within the FEA simulation can assist with the design of experiments for the CRM measurements. The CRM data presented in Fig. 4 was obtained from the oxide covered structure. Although optically transparent to CRM, the ILD0 and TEOS layers generate an equibiaxial stress ($\sigma_{x_s} = \sigma_{y_s}$) in the silicon that is the superposition of both thermal and intrinsic stresses. Athermal stresses are entirely dependent upon the processing history, but thermal contributions can be approximated using Eq. (14),

$$\sigma_m = \frac{E_m(\alpha_{si} - \alpha_m)(T - T_m)}{1 - \nu_m},$$

$$\sigma_{surface} = \frac{3(1 - \nu_{si}) \sum \sigma_m d_m}{d_{si}}, \tag{14}$$

where d_m is the layer thickness, T_m is the strain-free temperature for material m, and T is the temperature of interest. Because this stress is uniform across the wafer, there is no truly stress-free location on the surface of the Si to use as the reference peak. However, Eq. (14) gives a thermal contribution to the stress in the silicon at the oxide stack interface of only 0.5 MPa, which corresponds to a predicted Raman shift of 0.001 cm^{-1} and is significantly less than the ± 0.05 cm^{-1} 95% confidence interval of the peak position of the Pearson VII fit of the CRM measurements. Typical athermal stresses for PSG, USG, and TEOS are similarly small and are neglected. Given these considerations, the stress in the region away from the TSV is negligible, and because it exhibited consistent peak positions, this region was the reference peak position (ω_0). The FEA simulation predicts an approximately equibiaxial tensile stress of 15 MPa, which is larger than Eq. (14), but still below the ± 0.05 cm^{-1} uncertainty. The FEA simulation indicates that equilibrium film stress is reached about 30 μm from the TSV-Si interface. The experimental line scan range of 80 μm centered on the TSV was thus sufficient to capture the region in which a stress gradient was expected along with a significant portion of unstressed Si.

The successful prediction of the Raman shift—particularly for the oxide stack intact case (Fig. 5)—belies the complexity of an issue that is currently not being addressed in this or other works: the information volume of CRM can be large compared to the gradients in the strain field. In the present study, the FEA simulations calculate strain and predicted shift at integration points within the elements and then extrapolate these fields to nodes, including the nodes along the x_s axis. It is the values at these nodes that are plotted in Figs. 4–6 for comparison with the CRM measurements. As previously observed, because the gradient in the shift field in Fig. 3 is small over the $\approx$200 nm length scale that the CRM operates at, using surface nodes should produce accurate results. For less uniform shift fields, such as the one presented in Fig. 7, neglecting information volume effects is more problematic. To illustrate this, a gray ellipsoidal cross-section along the x_s axis of Fig. 7 is drawn to represent the information volume of the 405 nm laser (arbitrarily chosen to demonstrate the concept), with the bottom of the ellipse tangent with a 95 nm depth line (dashed). Away from the TSV, there are only small variations in the calculated Raman shift within the top 95 nm; however, near the TSV there is a 0.3 cm^{-1} gradient in the predicted Raman shift in the top 95 nm. Similar to the 6 to 1 convolution of the strain to shift prediction, consideration of the information volume would require field values from many elements to be consolidated into a single shift value, reducing a 3-D problem into a single scalar.

Because the correlation between the predicted and measured shifts for the oxide off case was not as strong as the oxide on case, electron backscattered diffraction (EBSD) was also attempted to gain a higher spatial resolution of the Si stress state around the TSV.[23] Since the oxide stack is not electron transparent, EBSD could only be performed on the oxide stack removed samples. Electron backscattered diffraction is also a surface sensitive technique; however, because it measures the 5 components of the deviatoric strain tensor, it has an advantage over CRM for evaluating complex stress states. Although previous comparisons between the two techniques have shown good agreement for simple stress states,[23] analysis of the complex stress state surrounding the TSV requires further work.

Regardless of the current limitations, the combination of the CRM measurements with the FEA simulations will be a useful tool for microelectronic device design—specifically for designing high density devices. A high spatial density of TSVs would allow the device to operate with greater bandwidths with less power; however, due to the stress field the TSV induces in the surrounding silicon, there is a balance between the achievable density and device reliability. Due to the increase in carrier mobility in strained silicon, an overlapping strain field from neighboring TSVs results in the potential to cause leakage current between TSVs. For the test structure investigated here, it appears that arrays of TSVs spaced at 60 μm is sufficient to prevent the strain fields of neighboring devices from strongly interacting. Although the array spacing is specific to the test structure studied, the methodology employed is more universally applicable.

V. CONCLUSIONS

CRM has been applied to a commercial silicon microelectronic feature to confirm the validity of the FEA simulated strain state. Because FEA simulation is an extremely useful tool for the development of new microelectronic and MEMS devices, the ability to predict Raman shifts from simulations and directly compare to measurements provides an excellent methodology for confirming the validity of the simulations. Although EBSD provides higher spatial resolution and the full deviatoric strain tensor, CRM can successfully and non-destructively measure strain in stressed silicon in a very robust set of conditions. This methodology can validate model geometry, material properties, and help to establish design guidelines for future 3-D integrated devices.

[1]P. Garrou, *Handbook of 3D Integration: Technology and Applications of 3D Integrated Circuits* (Wiley-VCH, Weinheim, 2008).
[2]S. F. Al-Sarawi, D. Abbott, and P. Franzon, IEEE Trans. Compon., Packag. Manuf. Technol., Part B **21**, 2 (1998).
[3]J. A. Davis, R. Venkatesan, A. Kaloyeros, M. Beylansky, S. J. Souri, K. Banerjee, K. C. Saraswat, A. Rahman, R. Reif, and J. D. Meindl, Proc. IEEE **89**, 305 (2001).
[4]A. W. Topol, D. C. L. Tulipe, L. Shi, D. J. Frank, K. Bernstein, S. E. Steen, A. Kumar, G. U. Singco, A. M. Young, K. W. Guarini, and M. Ieong, IBM J. Res. Dev. **50**, 491 (2006).
[5]P. Marchal, B. Bougard, G. Katti, M. Stucchi, W. Dehaene, A. Papanikolaou, D. Verkest, B. Swinnen, and E. Beyne, Proc. IEEE **97**, 96 (2009).
[6]C. C. Liu, I. Ganusov, M. Burtscher, and S. Tiwari, IEEE Des. Test **22**, 556 (2005).
[7]E. M. Chow, G. G. Yaralioglu, C. F. Quate, and T. W. Kenny, Appl. Phys. Lett. **80**, 664 (2002).
[8]N. M. Jokerst, M. A. Brooke, J. Laskar, D. S. Wills, A. S. Brown, M. Vrazel, S. Jung, Y. Joo, and J. J. Chang, IEEE J. Sel. Top. Quantum Electron. **6**, 1231 (2000).
[9]R. F. Figueroa, S. Spiesshoefer, S. L. Burkett, and L. Schaper, J. Vac. Sci. Technol. B **23**, 2226 (2005).
[10]R. Nagarajan, K. Prasad, L. Ebin, and B. Narayanan, Sens. Actuators, A **139**, 323 (2007).
[11]S. Spiesshoefer, Z. Rahman, G. Vangara, S. Polamreddy, S. Burkett, and L. Schaper, J. Vac. Sci. Technol. A **23**, 824 (2005).
[12]N. Lietaer, P. Storås, L. Breivik, and S. Moe, J. Micromech. Microeng. **16**, S29 (2006).

[13]C. Tsang, P. Andry, E. Sprogis, C. Patel, B. Webb, D. Manzer, and J. Knickerbocker, CMOS-Compatible Through Silicon Vias for 3D Process Integration, 26–30 November 2007 (Mater. Res. Soc. Symp. Proc., Boston, MA, 2007), pp. Y01-01.
[14]N. P. Pham, D. S. Tezcan, W. Ruythooren, P. De Moor, B. Majeed, K. Baert, and B. Swinnen, J. Micromech. Microeng. **18**, 125008 (2008).
[15]C. S. Selvanayagam, J. H. Lau, XZhang, S. K. W. Seah, K. Vaidyanathan, and T. C. Chai, in Electronic Components and Technology Conference, 27–30 May 2008 (Lake Buena Vista, FL), pp. 1073-1081.
[16]C. Okoro, Y. Yang, B. Vandevelde, B. Swinnen, D. Vandepitte, B. Verlinden, and I. de Wolf, in IEEE Internation Interconnect Technology Conference, 1–4 June 2008 (Burlingame, CA), pp. 16-18.
[17]T.-Y. Kuo, S.-M. Chang, Y.-C. Shih, C.-W. Chiang, C.-K. Hsu, C. K. Lee, C.-T. Lin, Y.-H. Chen, and W.-C. Lo, in Electronic Components and Technology Conference, 27–30 May 2008 (Lake Buena Vista, FL), pp. 853-858.
[18]N. Ranganathan, K. Prasad, N. Balasubramanian, and K. L. Pey, J. Micromech. Microeng. **18**, 075018 (2008).
[19]P. Morrow, B. Black, M. Kobrinsky, S. Muthukumar, D. Nelson, C.-M. Park, and C. Webb, in Design and Fabrication of 3D Microprocessors, 26–30 Nov 2007 (Mater. Res. Soc. Symp. Proc., Boston, MA, 2007), pp. Y03-02.
[20]A. P. Karmarkar, X. Xu, and V. Moroz, in IEEE International Reliability Physics Symposium, 26–30 April 2009 (Montreal, Canada), pp. 682-687.
[21]J. Burns, in Three Dimensional System Integration, edited by A. Papanikolaou, D. Soudris, and R. Radojcic (Springer, Boston, MA, 2011), pp. 13-32.
[22]D. Henry, J. Charbonnier, P. Chausse, F. Jacquet, B. Aventurier, C. Brunet-Manquat, V. Lapras, R. Anciant, N. Sillon, B. Dunne, N. Hotellier, and J. Michailos, in IEEE International Electronics Packaging Technology Conference, 28–31 July 2008 (Singapore), pp. 35–44.
[23]M. D. Vaudin, Y. B. Gerbig, S. J. Stranick, and R. F. Cook, Appl. Phys. Lett. **93**, 193116 (2008).
[24]G. J. Leusink, T. G. M. Oosterlaken, G. C. A. M. Janssen, and S. Redelaar, Thin Solid Films **228**, 125 (1993).
[25]Y. B. Gerbig, S. J. Stranick, and R. F. Cook, Scr. Mater. **63**, 512 (2010).
[26]M. J. Pelletier, Analytical Applications of Raman Spectroscopy, (Blackwell Malden, MA, USA, 1999).
[27]W. H. Weber and R. Merlin, Raman Scattering in Materials Science (Springer, New York, 2000).
[28]E. Anastassakis, A. Pinczuk, E. Burstein, F. H. Pollak, and M. Cardona, Solid State Commun. **8**, 133 (1970).
[29]E. Anastassakis, A. Cantarero, and M. Cardona, Phys. Rev. B **41**, 7529 (1990).
[30]T. Miyatake, A. A. Porporati, and G. Pezzotti, J. Appl. Phys. **105**, 113514 (2009).
[31]E. Bonera, M. Fanciulli, and D. N. Batchelder, J. Appl. Phys. **94**, 2729 (2003).
[32]I. De Wolf, H. E. Maes, and S. K. Jones, J. Appl. Phys. **79**, 7148 (1996).
[33]I. De Wolf and E. Anastassakis, J. Appl. Phys. **85**, 7484 (1999).
[34]V. T. Srikar, A. K. Swan, M. S. Unlu, B. B. Goldberg, and S. M. Spearing, J. Microelectromech. Syst. **12**, 779 (2003).
[35]M. Komatsubara, T. Namazu, Y. Nagai, S. Inoue, N. Naka, S. Kashiwagi, and K. Ohtsuki, Jpn. J. Appl. Phys. **48**, 04C021 (2009).
[36]T. Wermelinger, C. Charpentier, M. D. Yüksek, and R. Spolenak, J. Raman Spectrosc. **40**, 1849 (2009).
[37]See supplementary material at http://dx.doi.org/10.1063/1.3644971 for an in depth description of the Raman-FEA implementation, and the code used.